Revealing Urban Deformation Patterns through InSAR Time Series Analysis with TCN and Transfer Learning

Mengshi Yang[1,2], Saiwei Li[1], Hang Yu[1], Hao Wu[1], Menghua Li[3]

[1] Yunnan University, China, People's Republic of;
[2] Yunnan International Joint Laboratory of China-Laos-Bangladesh-Myanmar Natural Resources Remote Sensing Monitoring, China, People's Republic of;
3 Kunming University of Science and Technology,China, People's Republic of

Keywords: InSAR Time Series, Deformation, Built Environment, Data-Drive, TCN.

Abstract

Current multi-epoch InSAR techniques heavily rely on the assumption of linear deformation. This can sometimes overlook crucial deformation signals when using velocities for evaluation. The process of interpreting InSAR time series is not only time-consuming and labor-intensive but also requires a certain level of expertise. This study refines existing InSAR deformation categories, such as stable, linear, step, piecewise linear, power, and undefined, to define 'canonical deformation time series patterns.' We propose an innovative approach for InSAR post-processing using Temporal Convolutional Networks (TCN) and transfer learning. Due to the limited availability of real data, we use simulated data to train a pre-existing model. We then assess the effectiveness of our method in identifying urban deformation patterns. This research could significantly improve our understanding of large-scale InSAR time series deformation and reveal the underlying patterns.

1. Introduction

Spaceborne InSAR technology, with its all-day, all-weather, large-scale observation capabilities, has become a crucial tool for monitoring ground deformation. Overcoming traditional InSAR technology's limitations—such as issues with time de-coherence and atmospheric delay effects—time-series InSAR technology enables high-precision monitoring of ground deformation. However, the existing time-series InSAR technology operates on a linear deformation assumption, estimating ground deformation using a rate index. Consequently, potentially dangerous deformation signals like sudden deformation or deformation acceleration are retained in the time-series deformation during the observation period. The time-series InSAR dataset can supply millions of points for hundreds of observational moments of deformation. However, identifying InSAR time series deformation relies on manual interpretation, which is not only time-consuming and laborious but also requires expert knowledge. In order to address these issues, a number of machine learning and multiple hypothesis testing methods have been proposed.

Clustering algorithm is an unsupervised machine learning algorithms that divide a dataset into several subsets without prior knowledge. It has widely used for exploring deformation patterns in InSAR time series. Clustering algorithms such as SOM (Li and Ke 2015), k-means (Gagliardi et al. 2021), and DBSCAN (Schneider and Soergel 2021) have all been utilized for clustering InSAR time series data of the Earth's surface, enabling the analysis of spatiotemporal heterogeneity. However, a limitation of this approach is that the clustering outcomes are all linear trends, differing primarily in their rates of subsidence. Subsequently, clustering the vertical and horizontal components of deformation from LOS InSAR enhances the interpretability of the clustering results.(Schlögl, Widhalm, and Avian 2021)(Festa et al. 2022). Since the results of clusters are often unknown, obtaining interpretable outcomes requires multiple experiments to adjust the final number of clusters. To some extent, this issue can be addressed by conducting principal component analysis before clustering (Festa et al. 2023) or performing hypothesis testing on clusters after clustering(Zhu, Hu, and Xu 2023). Compared to clustering InSAR time series, the classification of InSAR time series with predefined categories is easier to interpret. The earliest study on classifying potential patterns in InSAR time series aimed to detect deformation patterns of landslides. This study employed multiple hypothesis testing methods to categorize regional deformations into six types: uncorrelated, linear, quadratic, bilinear, discontinuous with constant velocity, and discontinuous with varying velocity(Berti et al. 2013). Subsequently, InSAR phase unwrapping errors (PUE) are included as a new category that requires hypothesis testing.(Mirmazloumi, Wassie, et al. 2022). Although multiple hypothesis testing methods can achieve good results, they require more specialized knowledge in the field of InSAR. Furthermore, with the enhanced ground observation capabilities of SAR satellites and the increasing volume of InSAR data, computational resource consumption is becoming increasingly high. Therefore, several supervised learning methods have been proposed for the classification of InSAR time series. Artificial Neural Networks (ANN)(Mirmazloumi, Gambin, et al. 2022), Long Short-Term memory(LSTM)(Kulshrestha, Chang, and Stein 2022)(Tiwari and Shirzaei 2024), and Sparse_AutoEncoder-Convolutional neural networks(SAE-CNN)(Li et al. 2023) have been proposed for mining potential patterns in large-scale InSAR time series data. However, these methods often require a large amount of manually labeled real deformation data from the ground surface. Since InSAR time series exhibit complex deformation patterns, labeling sample data is even more challenging in areas with small deformations and noise interference.

This study was initiated by defining what we term 'canonical deformation time series patterns', drawing upon our understanding of urban deformation and our expertise with InSAR data analysis. We have refined the previously proposed InSAR deformation pattern categories, expanding the bilinear pattern into piecewise linear, replacing quadratic deformation patterns with power deformation, and introducing a new 'undefined' category to encompass complex InSAR deformations. This results in a total of six deformation patterns: stable, linear, step, piecewise linear, power, and undefined. Subsequently, we propose an innovative approach for InSAR post-processing, which involves exploring deformation time series using Temporal Convolutional Networks (TCN) and transfer learning techniques. Additionally, we address the challenge posed by limited real, ground-labeled InSAR data by leveraging simulated data to construct a pre-trained model. Finally, we evaluate the efficacy of our proposed method in accurately identifying deformation patterns in urban

environments. The paper is organized as follows: Section 2 delineates the employed methods. Section 3 elucidates the research data. Section 4 presents the results and discussions, while Section 5 concludes the study.

2. Methodology

In this study, six deformation patterns in InSAR time series are identified, drawing upon insights from previous research on urban deformation and experiences in annotating real data. The Savitzky-Golay filter and Temporal Convolutional Network (TCN) were employed together to extract deformation features from the InSAR deformation time series. Furthermore, a transfer learning method was utilized to enhance the effectiveness of deformation pattern recognition.
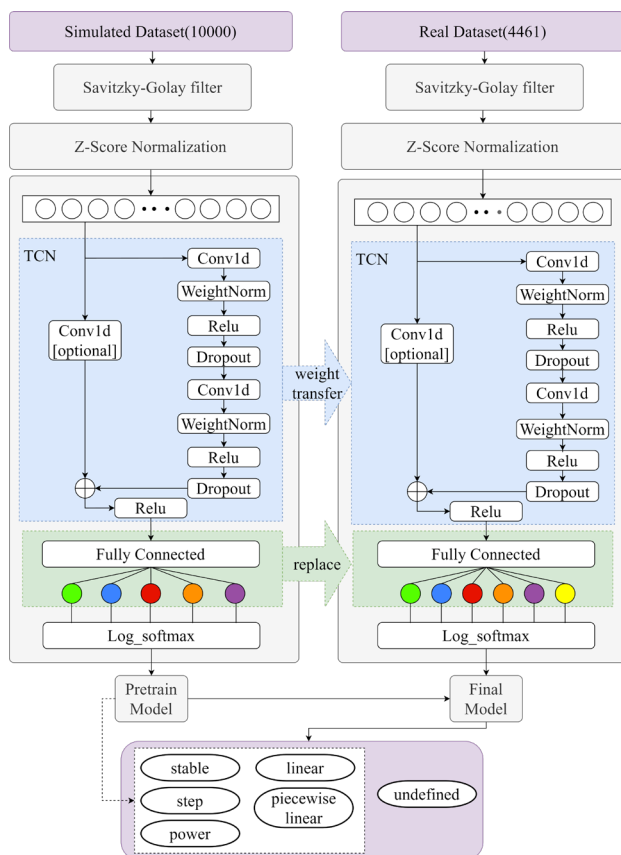

Figure 1. Framework of this study

2.1 Canonical Time Series Deformation Patterns

Our approach classifies time series deformation patterns into predefined types. These types are identifiable in any InSAR time series dataset and can be interpreted based on their associated physical processes. Six deformation patterns are defined: stable, linear, step, piecewise linear, power, and undefined.

⬥ **Stable**: The mathematical meaning of this deformation pattern is that the InSAR deformation is unrelated to time in the time series, and the deformation amount generally fluctuates randomly around a constant value. Physically, it usually represents stable InSAR coherent points with no significant deformation during the monitoring period(Berti et al. 2013).

⬥ **linear**: The mathematical meaning of this deformation pattern is that the InSAR deformation varies linearly with time at a constant rate, either increasing or decreasing. Physically, it is

often associated with long-term ground deformation processes such as settlement.

⬥ **Step**: Its mathematical meaning is that the deformation velocity of InSAR undergoes a displacement step at a certain moment, indicating the existence of a jump-type discontinuity at that moment. The velocity before and after the step may be similar or change(Berti et al. 2013). Since some instantaneous events only cause one or multiple jumps on the surface, their physical meanings are related to activities such as earthquakes, fault slips, mining operations, and so on.

⬥ **Piecewise Linear**: This term refers to the division of the InSAR deformation time series into several linear domains with varying velocities, connected by segmentation points. When surface motion characteristics are directly linked with water or hydrocarbon reserves, the deformation pattern can be modeled as a combination of several different linear functions over a specific time period(Ketelaar 2009). In practical terms, bilinear and trilinear models are relatively common. For instance, during oil or natural gas extraction, a segmentation point can be established, with different linear domains potentially existing before and after this point.

⬥ **Power**: Mathematically, the InSAR deformation velocity signifies a trend characterized by varying deformation rates that change continuously over time. Physically, this is often linked to post-earthquake deformation(Savage, Svarc, and Prescott 2003) , gradual deformation of landslides (Montgomery, Sullivan, and Greenberg 1998), , soil settlement or compaction processes (Wang, Deng, and Zheng 2020), and gradual deformation in mining areas.

⬥ **Undefined**: The deformation patterns in MT-InSAR can be quite complex. In addition to the five basic patterns mentioned earlier, there may also be low-quality time series due to processing errors, mixed sequences involving various basic patterns, and other complex patterns that do not align with the characteristics of the basic patterns.

2.2 Deformation Patterns Recognition based on TCN and Transfer Learning

In this section, the methodology of Temporal Convolutional Network (TCN) and Transfer Learning is introduced, adapted for InSAR time series analysis.

Convolutional Neural Network (CNN) naturally possess the advantage of parallel processing, which can shorten the computation time. Although traditional CNN lack the ability to retain historical information, specifically designed CNN can still achieve good performance in time series analysis. Temporal Convolutional Network (TCN)(Bai, Kolter, and Koltun 2018) are a special type of CNN that can be used for modeling sequential problems. When dealing with InSAR deformation sequences, TCN treat them as one-dimensional objects (1×n matrices). Through multi-layer causal convolutions, TCN can obtain a large enough receptive field and trace historical information. Although this approach can make the neural network very deep, dilated convolutions can reduce the number of layers while maintaining the receptive field, saving a significant amount of time(Oord et al. 2016). Additionally, TCN benefit from the advantage of massive parallel processing.The hidden layer of a TCN is a basic module called TemporalBlock (Figure 1). The input to a TemporalBlock is a one-dimensional time series. The TemporalBlock mainly consists of two convolutional layers with the same dilation factor. Conv1d represents a one-dimensional dilated causal convolution. The WeightNorm layer is used to normalize the weight parameters and accelerate model training. The ReLU layer serves as a nonlinear activation function, enhancing the model's expressive ability. The Dropout layer is employed to prevent overfitting in

deep learning models. The input InSAR deformation time series x undergoes two layers of dilated causal convolutions and is then passed through a residual connection to output the current hidden state h(x).

Transfer Learning is a machine learning approach that focuses on transferring knowledge learned from a solved task A to a related new task B, thereby aiding in the resolution of task B. This is particularly useful when data for task B is limited or difficult to obtain. The core objective of transfer learning is to leverage the accumulated experience from the source task to enhance the learning efficiency and performance of the target task.

3. Experiments Data

Our experimental data comprises both simulated and real data. The simulated data is utilized for pre-training, while the real data is employed for fine-tuning the model through transfer learning.

3.1 Simulated Data

The construction of simulated data is primarily based on the primary deformation patterns mentioned in section 2.1. The temporal InSAR deformation simulations are primarily calculated using the following formula, which is derived from the mathematical significance of these patterns:

$$D_t = f(t) + n(t), \quad n(t) \sim N(0, 0.83^2) \quad (1)$$

In formula (1), D_t represents the InSAR deformation amount at time for a particular Persistent Scatterer (PS) point. To adequately simulate the characteristics of real data, Gaussian white noise is added to the simulated data. In this study, the Gaussian white noise follows a standard normal distribution with a mean of 0 and a variance of 0.83^2. This noise addition helps to mimic the inherent randomness and uncertainty present in real-world InSAR measurements, thereby enhancing the realism and reliability of the simulated data for pre-training purposes. In our study, the simulated data used for pre-training only needs to conform to the pre-defined first five deformation patterns (Figure. 2).
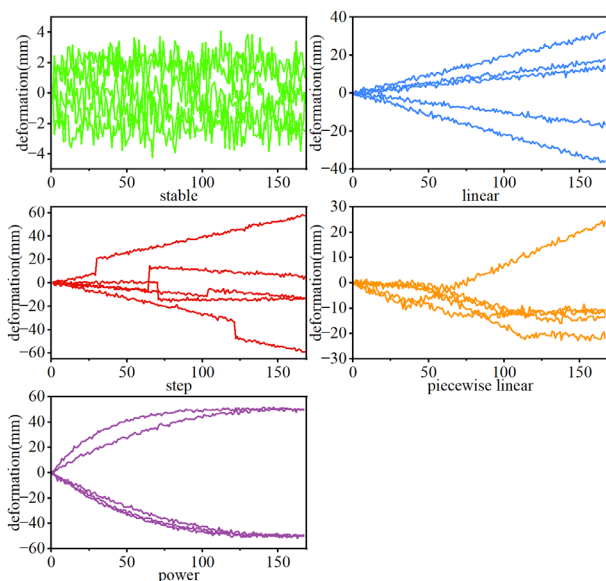

Figure 2 Simulated deformation time series.

3.2 Real Data

The real data employed in our study is derived from Sentinel-1 and covers a rectangular region near Kunming City, China. Kunming is situated in the north of the Yunnan province, with coordinates ranging from 102°10′ to 103°40′E and 24°23′ to 26°22′N. Karst landforms dominate the study area, and lithologically silty and soft clay constitute the primary soil structure(Guo et al. 2020). Kunming is one of the cities in western China that exhibits relatively significant surface subsidence. The Sentinel-1 data provides valuable insights into the deformation patterns and subsidence characteristics of the region, enabling us to conduct accurate and reliable analysis for our research objectives.
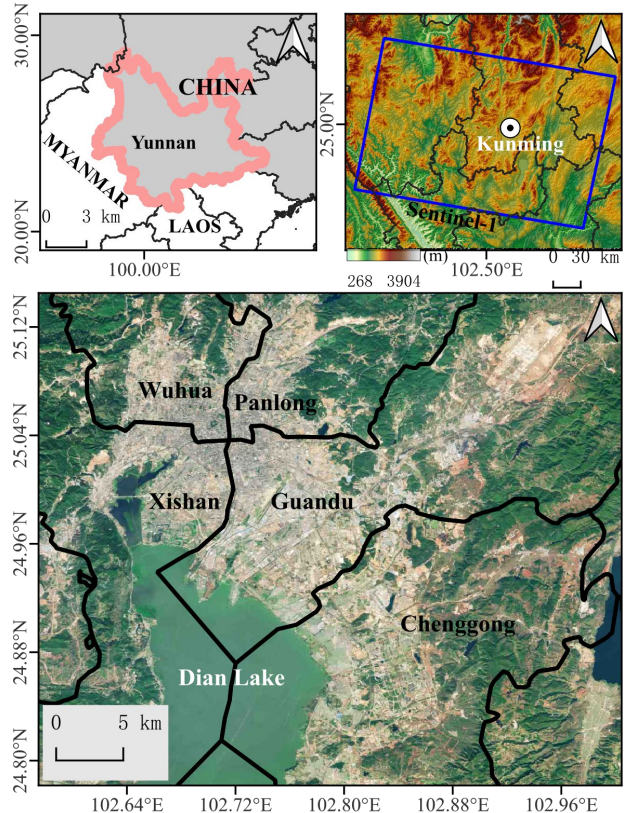

Figure 3 The top left figure shows the location of Yunnan province. The top right figure presents the collected SAR coverages, depicted with the topography of Kunming. The bottom figure displays the central districts of Kunming city.

After processing the Sentinel-1 data using PS-InSAR techniques, we obtained 2,378,751 Persistent Scatterer (PS) time series. Each time series comprises 168 timestamps, representing deformations measured in millimeter resolution along the line of sight. For the purpose of transfer learning, we labeled 3566 points as the training set, while 895 points were designated as the test set for the real data. The ratio between the training and test sets is 8:2, ensuring a balanced and representative distribution of data for model training and evaluation (Table1).

Patterns	Train	Test
stable	600	151
linear	595	149
step	592	149
Piecewise linear	596	150
pow	595	149
undefined	588	147

Table 1 Real dataset partitioning.

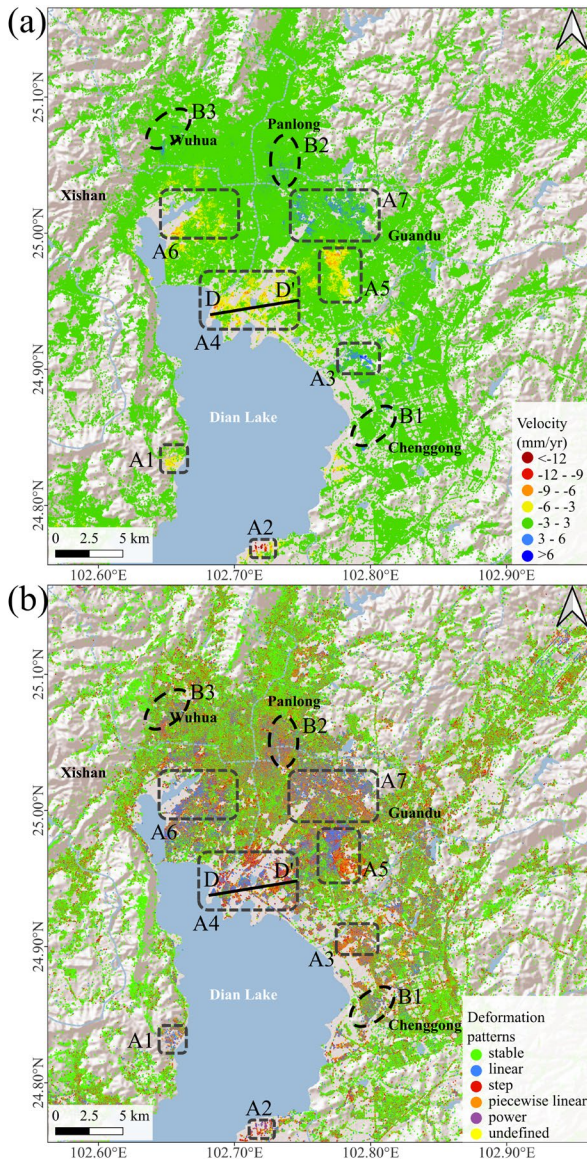## 4. Results And Discussion

4.1 Results

Figure 4 (a) represents a deformation velocity map of Kunming City, while (b) represents a deformation pattern map of Kunming City. A1 to A7 are deformation zones that can be clearly identified from the deformation rate map. Conversely, B1 to B3 are deformation zones that are difficult to discern from the deformation rate map but can be easily identified from the deformation pattern map. The line DD' traverses a key subsidence area along the shores of Dianchi Lake.

Fig.4(a) shows the deformation velocity in Kunming City with the deformation velocity of most points(3σ) ranging from -5 to 5 mm/year, as shown in Fig.5. The key subsidence areas are concentrated along the shores of Dian Lake, with a few areas experiencing uplift. Fig.4(b) illustrate the identified deformation patterns in the study area, and various deformation patterns are also observed in other areas with lower velocity in the velocity map given in Fig.4(a). A1 experiences slight subsidence, primarily characterized by linear and piecewise linear deformation patterns. A2 exhibits more severe subsidence, with deformation patterns including piecewise linear, step, and power modes. A3 undergoes slight uplift, mainly in a piecewise linear mode, possibly related to self-built housing in the area.

A4 is a key subsidence area around the Dianchi International Convention and Exhibition Center, encompassing various subsidence patterns. A5 is the xiaobanqiao key subsidence area, where severely subsiding regions are dominated by linear subsidence, while regions with slower subsidence show a mix of piecewise linear and step subsidence patterns. A6, located along the lake, experiences severe subsidence primarily in a linear mode. A7 is the area with the most severe uplift in Kunming City, associated with linear and piecewise linear deformation patterns. Regions B1, B2, and B3 appear relatively stable in the velocity map, but our analysis reveals that their deformation patterns remain complex.
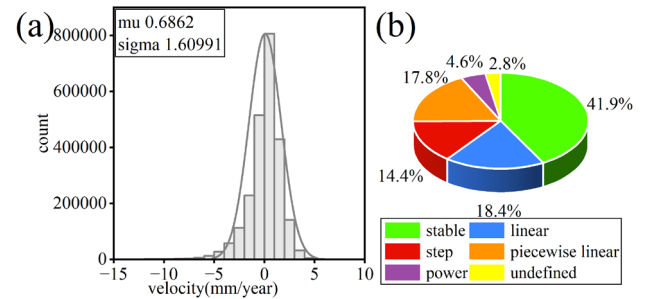

Figure 5 (a) demonstrates the distribution of ground deformation rates across Kunming City, while (b) illustrates the proportion of various deformation patterns throughout Kunming City.

In region A4, the cross-section DD' traverses a severe subsidence area along the northern shore of Dianchi Lake. As the distance extends from the lakeside to the land, the surface elevation gradually increases, with a change of approximately 45 meters. In areas with higher elevations, the deformation rates are smaller, and there are more instances of stable deformation patterns. in contrast, lower elevations are dominated by non-stable deformation. Within a distance of 0 to 4000 meters from the lake, linear subsidence patterns are most common. Between 4000 and 6000 meters from the lake, piecewise linear subsidence patterns prevail. Within 7000 to 8000 meters from the lake, there are tall building clusters, and most of the deformation patterns within these clusters are stable. Finally, within 9000 to 11000 meters from the lake, the deformation patterns are primarily step subsidence (Fig. 6).
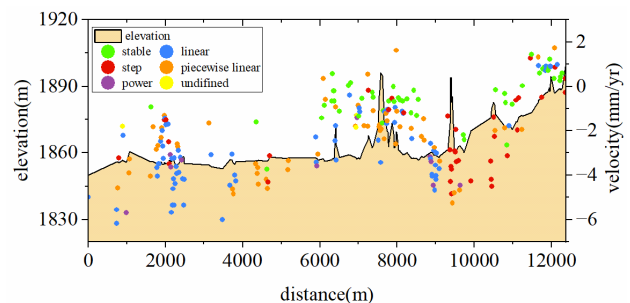

Figure 6 Changes in elevation, deformation rate, and deformation patterns along the DD' line (Figure. 4).
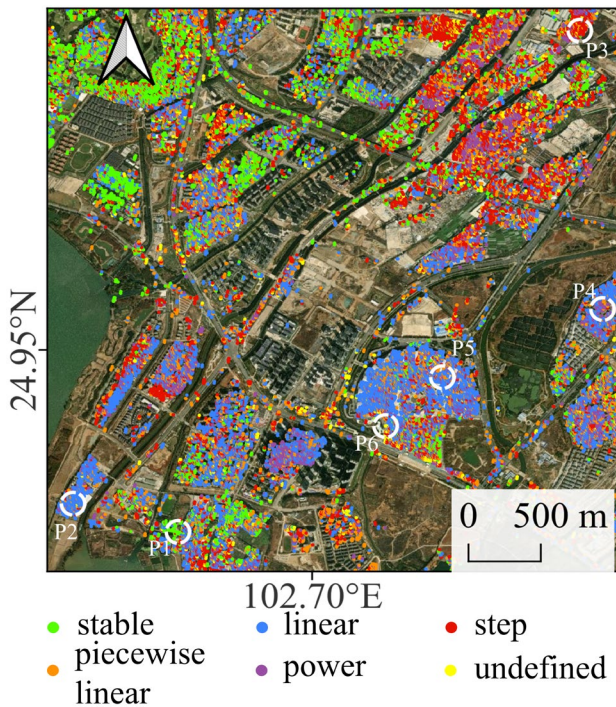
Figure 7 The detail deformation patterns map of area A4. The p1 to p6 represent the main clustering areas for stable, linear, step, piecewise linear, power, and undefined deformation patterns, respectively.

Figure 8 S1-S6 represent the main deformation patterns in the region from P1 to P6 in Fig. 7.

In the key subsidence area A4, we selected typical regions P1 to P6 (Fig. 7). We plotted their main deformation time series S1 to S6 (Fig. 8). S1 indicates that region P1 experiences stable deformation patterns. S2 demonstrates that region P2 exhibits a linear subsidence pattern with a cumulative settlement of up to 40mm in six years. S3 reveals that region P3 is primarily characterized by a step deformation mode, with an instantaneous step of 10mm occurring around September 2018. S4 shows that region P4 is dominated by a piecewise linear deformation pattern, which can be divided into three linear segments. The first linear segment, from January 2017 to March 2018, has a relatively small settlement rate. The second segment, from April 2018 to October 2020, exhibits a higher settlement rate, possibly due to intense human engineering activities. The third segment, from October 2020 to December 2022, approaches a stable deformation rate. S5 represents region P5, which experiences a power deformation mode with a cumulative settlement of approximately 50mm. The deformation rate gradually decreases during the monitoring period and may stabilize in the future. This pattern may be related to changes in groundwater in the area. S6 indicates that the InSAR deformation in region P6 is a deformation mode beyond the five typical ones. The InSAR time series in this region is significantly affected by noise and exhibits a complex deformation pattern. Before September 2020, the deformation approximated a power decrease, followed by a large step change around September 2020, and then stabilized.
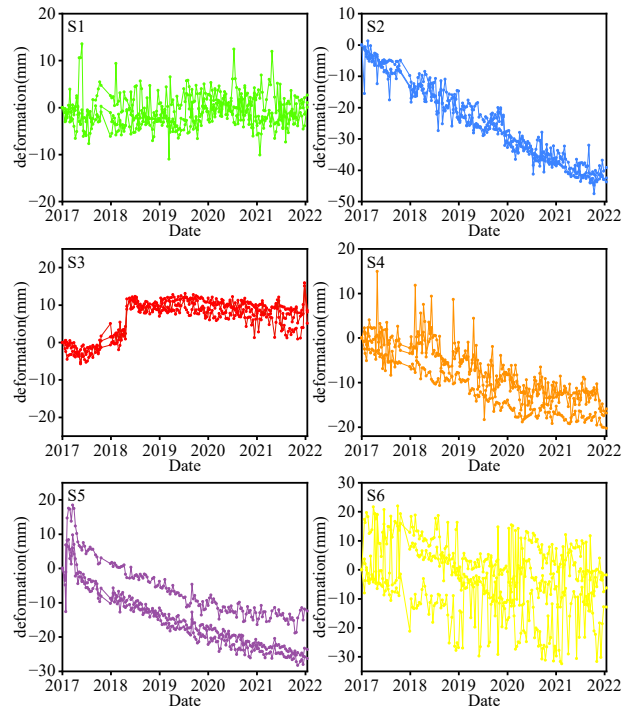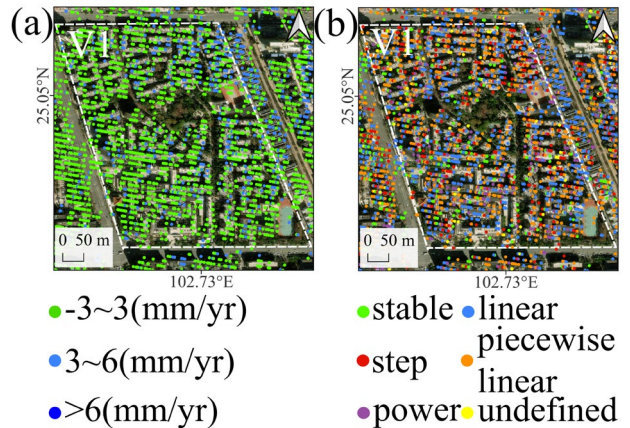

Figure 9 (a) represents the deformation rate in the V1 region, and (b) represents the deformation pattern in the V1 region.

In the B2 region (Figure 4), we selected the V1 neighborhood (Fig. 9) to explore its deformation patterns. Although the deformation rates in this area are relatively small, the deformation patterns remain complex. We plotted five typical InSAR deformation pattern clusters, S1 to S5 (Fig. 10), for this neighborhood. The upper and lower boundaries of each cluster represent the maximum and minimum deformation values observed at that particular time, respectively, while the balck line in the middle indicates the median deformation value for that time. Evidently, S1 represents a stable deformation pattern, with deformations fluctuating randomly around zero. Due to noise, even stable deformations can exhibit significant jumps, resulting in a range of approximately 40mm. S2 corresponds to a linear deformation pattern cluster, showing a lift of approximately 5 to 10mm over the monitoring period. S3 comprises step deformation patterns, with potential step moments occurring in May 2018, January 2020, July 2021, and January 2022. The variation in step moments across different time series within

a small area suggests that these steps may be caused by surface human activities rather than underlying physical processes. S4 represents a piecewise linear deformation pattern. The first linear segment, from January 2017 to May 2018, is relatively stable. The second segment, from May 2018 to March 2021, exhibits a higher rate of uplift. Finally, the third segment indicates a decrease in the uplift rate compared to the second segment. S5 depicts a power deformation pattern. The median InSAR deformation rates generally show an increasing trend over the six-year period. Additionally, the maximum values suggest that the corresponding surface coherent points undergo seasonal fluctuations during the power uplift process.
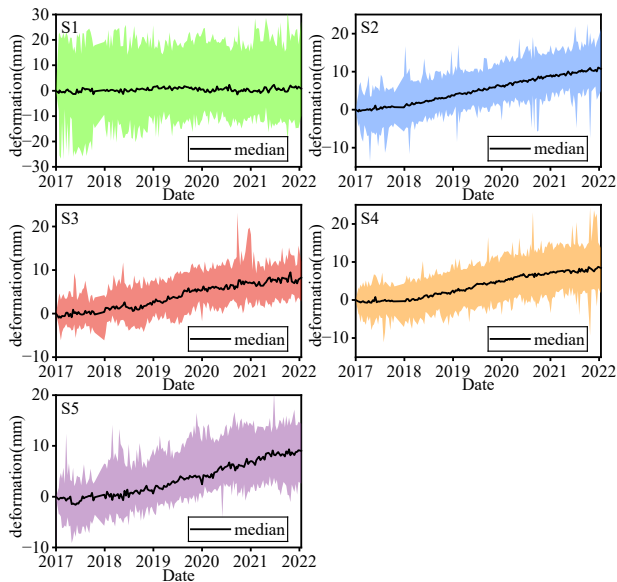

Figure 10 S1-S6 represent the InSAR Deformation Time Series Cluster in the region of Fig. 10 V1.

we analyze the relationship between different InSAR deformation patterns, deformation velocity, and coherence for all coherent points. Fig. 11 (a) reveals that most deformation patterns exhibit velocities concentrated between -5 and 5 mm/year, consistent with the overall velocity distribution.

Non-stable deformation patterns show a higher density of velocity distribution between Q2 and Q3 compared to Q1 and Q2. Negative velocities are more scattered among outlier data points compared to positive velocities.

Stable deformation points have a unimodal distribution with velocities ranging from -5 to 5 mm/year, peaking near 0 mm/year. Linear, piecewise linear, and power deformation patterns show a bimodal distribution with peaks in both positive and negative velocity segments. Median velocities for linear and piecewise linear deformations are greater than 0 mm/year, while for power deformations, it is less than 0 mm/year. Step and undefined deformation patterns also exhibit a bimodal distribution with medians near 0 mm/year, and a significant density of data points near 0 mm/year.

From Fig 11 (b), Coherence values for each deformation pattern are concentrated between 0.6 and 1, with medians falling within the range of 0.6 to 0.8.Outlier coherence values for each deformation pattern are clustered between 0 and 0.3. Stable deformation pattern has the highest density of data points between 0.6 and 0.8.Linear, piecewise linear, and power-law deformation patterns show similar coherence distribution shapes, with the highest concentration of data points between 0.8 and 1.Step and undefined deformation patterns also exhibit similar

coherence distribution shapes, with the highest density of data points between 0.7 and 0.9.
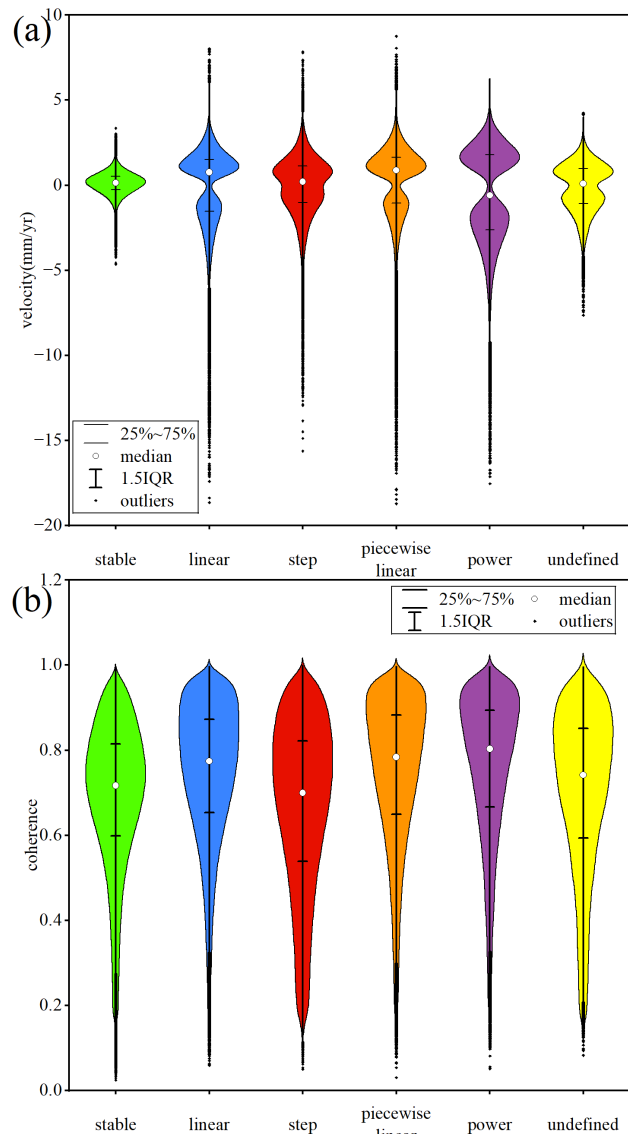

Figure 11 (a) displays the distribution of deformation rates for different patterns in Kunming City, while (b) illustrates the distribution of coherence for different patterns.

These observations suggest that different deformation patterns exhibit distinct characteristics in terms of their velocities distributions and coherence values. Stable deformations tend to have low rates and high coherence, while other deformation patterns, such as linear, piecewise linear, and power, may exhibit a wider range of velocity and varying degrees of coherence. Step and undefined deformation patterns show more variability in their velocity distributions but tend to have similar coherence levels. These observations provide valuable insights into the characteristics and underlying mechanisms of deformation in the studied areas, which can contribute to better understanding the geological processes driving these deformations.

4.2 Discussion

The results of our study demonstrate that the proposed method is highly effective in exploring the temporal deformation of the built environment using InSAR time series and uncovering potential patterns. This notable achievement is primarily attributed to the deep learning model we have constructed. In the following, we delve into the training specifics of the deep learning model, evaluate its performance, and identify areas for potential improvement.

Hyperparameter	Search space
Learning rate	1e-1,1e-2,1e-3
Batch size	16,32,64,128,256
Hidden layers	[1,10]
Hidden layer neurous	15,25,50,100,168,200,301,400
Dropout	0.01,0.05,0.01,0.5

Table 2 hyperparameters search space in this experiment.

4.2.1 Model hyperparameters: For deep learning models, hyperparameter adjustment is crucial, often determining the success or failure of a given task. Regarding the TCN neural network selected for our research, there are no available model parameters for reference in the context of InSAR time series classification. Therefore, we identified a set of commonly used empirical hyperparameter search spaces (Table 2). Initially, we randomly sampled each hyperparameter value range within the search space to construct hyperparameter combinations, resulting in 4800 unique combinations. Subsequently, we employed real data and utilized a random search approach (Bergstra and Bengio 2012) to conduct extensive exploratory training of the model. Through this process, we ultimately identified a relatively effective set of hyperparameters. Our model's initial learning rate is set to 0.001, and a learning rate decay strategy is adopted, where the learning rate is reduced to 10% of its current value every 10 epochs. The batch size is set to 256, with 10 hidden layers, 100 neurons per hidden layer, and a dropout rate of 0.05. As for the optimizer, we chose the Adam optimizer, which is relatively insensitive to hyperparameter settings and can yield similar results within a wide range of hyperparameters, facilitating the adjustment process.

4.2.2 Model performance: Equations must be numbered consecutively throughout the paper. The equation number is enclosed in parentheses and placed flush right. Leave one blank lines before and after equations:
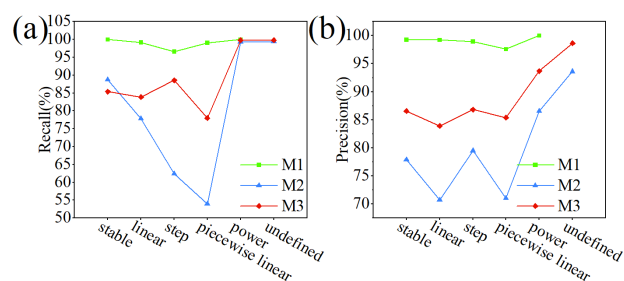

Figure 12 (a) displays the recall rates of different experimental methods, while (b) shows their precision rates. M1 represents training the model with simulated data and testing it with simulated data. M2 represents directly training the model with real data and testing it with real data. M3 represents training the model with simulated data, performing transfer learning with real data, and then testing it with real data.

Our study compares the performance differences among models trained under three distinct scenarios. We denote the five-class classification pretrain model trained directly on simulated data as M1, the six-class classification model trained directly on real data as M2, and the model that undergoes pre-training on simulated data followed by transfer learning and fine-tuning on real data as M3. Model M1 is designed specifically for five-class tasks and must be tested using simulated data. In contrast, M2 and M3 are evaluated using real data. The final accuracy rates are as follows: M1 achieves 99.1%, M2 achieves 80.3%, and M3 achieves 89.3%. Notably, M1 exhibits the highest recall and precision rates, validating the TCN model's effectiveness in recognizing deformation patterns from simulated InSAR time series data. Compared to M2, M3 demonstrates significant improvements in recall rates for linear, step, and piecewise linear deformation patterns. Additionally, M3 outperforms M2 in precision rates across all deformation modes (Fig. 12). These results suggest the feasibility of our proposed approach, which involves pre-training on simulated data followed by transfer learning on limited real data. The pre-trained model acquires the ability to represent features from simulated time series, and through weight transfer, the model initializes with a certain capability to extract features from real time series data. Consequently, the model converges more easily to a superior performance.

While the recall rates of M3 for stable, linear, and step deformation patterns range from 80% to 90%, its recall rate for piecewise linear patterns is only 78%, indicating room for improvement. Future research could explore enhancing the model's performance by increasing the number of training samples from real data and diversifying the samples for each deformation mode, ultimately leading to further improvements in model accuracy.

5. Conclusion

This study employs deep learning techniques to extract deformation patterns from extensive InSAR time-series data. Initially, a pre-trained model is trained using simulated data, followed by fine-tuning with real data through transfer learning. The resulting TCN deformation pattern recognition model, capable of six-class classification, exhibits high accuracy when applied to real datasets. Particularly, the model proves effective in detecting deformations in Kunming City. This research is instrumental in efficiently analyzing large-scale InSAR time-series data, offering valuable insights for deformation analysis and monitoring.

References

Bai, Shaojie, J Zico Kolter, and Vladlen Koltun. 2018. An Empirical Evaluation of Generic Convolutional and Recurrent Networks for Sequence Modeling. arXiv. https://doi.org/10.48550/arXiv.1803.01271.

Bergstra, James, and Yoshua Bengio. 2012. Random Search for Hyper-Parameter Optimization. Journal of Machine Learning Research 13 (January): 281–305.

Berti, M., A. Corsini, S. Franceschini, and J. P. Iannacone. 2013. Automated Classification of Persistent Scatterers Interferometry Time Series. Natural Hazards and Earth System Sciences 13 (8): 1945–58. https://doi.org/10.5194/nhess-13-1945-2013.

Festa, Davide, Manuela Bonano, Nicola Casagli, Pierluigi Confuorto, Claudio De Luca, Matteo Del Soldato, Riccardo

Lanari, et al. 2022. Nation-Wide Mapping and Classification of Ground Deformation Phenomena through the Spatial Clustering of P-SBAS InSAR Measurements: Italy Case Study. ISPRS J. Photogramm. Remote Sens 189 (July): 1–22. https://doi.org/10.1016/j.isprsjprs.2022.04.022.

Festa, Davide, Alessandro Novellino, Ekbal Hussain, Luke Bateson, Nicola Casagli, Pierluigi Confuorto, Matteo Del Soldato, and Federico Raspini. 2023. Unsupervised Detection of InSAR Time Series Patterns Based on PCA and K-Means Clustering. International Journal of Applied Earth Observation and Geoinformation 118 (April): 103276. https://doi.org/10.1016/j.jag.2023.103276.

Gagliardi, Valerio, Fabio Tosti, Luca Bianchini Ciampoli, Fabrizio D'Amico, Amir M. Alani, Maria L. Battagliere, and Andrea Benedetto. 2021. Monitoring of Bridges by MT-InSAR and Unsupervised Machine Learning Clustering Techniques. In Earth Resources and Environmental Remote Sensing/GIS Applications XII, edited by Karsten Schulz, Konstantinos G. Nikolakopoulos, and Ulrich Michel, 16. Online Only, Spain: SPIE. https://doi.org/10.1117/12.2597509.

Guo, Shipeng, Yongjie Ji, Xin Tian, Wangfei Zhang, Wei Kang, Yun Li, and Tingwei Zhang. 2020. Deformation Velocity Monitoring in Kunming City Using Ascending and Descending Sentinel-1A Data with SBAS-InSAR Technique. In IGARSS 2020 - 2020 IEEE International Geoscience and Remote Sensing Symposium, 1993–96. Waikoloa, HI, USA: IEEE. https://doi.org/10.1109/IGARSS39084.2020.9324650.

Ketelaar, V. B. H. 2009. Satellite Radar Interferometry: Subsidence Monitoring Techniques. Vol. 14. Springer Science & Business Media.

Kulshrestha, Anurag, Ling Chang, and Alfred Stein. 2022. Use of LSTM for Sinkhole-Related Anomaly Detection and Classification of InSAR Deformation Time Series. IEEE Journal of Selected Topics in Applied Earth Observations and Remote Sensing 15: 4559–70. https://doi.org/10.1109/JSTARS.2022.3180994.

Lanari, R, P Berardino, M Bonano, F Casu, A Manconi, M Manunta, M Manzo, et al. 2010. Surface Displacements Associated with the L'Aquila 2009 Mw 6.3 Earthquake (Central Italy): New Evidence from SBAS-DInSAR Time Series Analysis. Geophys. Res. Lett. 37 (October). https://doi.org/10.1029/2010GL044780.

Li, Menghua, Hanfei Wu, Mengshi Yang, Cheng Huang, and Bo-Hui Tang. 2023. Trend Classification of InSAR Displacement Time Series Using SAE–CNN. *Remote Sens* 16 (1): 54. https://doi.org/10.3390/rs16010054.

Mirmazloumi, S. Mohammad, Angel Fernandez Gambin, Riccardo Palamà, Michele Crosetto, Yismaw Wassie, José A. Navarro, Anna Barra, and Oriol Monserrat. 2022. Supervised Machine Learning Algorithms for Ground Motion Time Series Classification from InSAR Data. *Remote Sens* 14 (15): 3821. https://doi.org/10.3390/rs14153821.

Mirmazloumi, S. Mohammad, Yismaw Wassie, José Antonio Navarro, Riccardo Palamà, Vrinda Krishnakumar, Anna Barra, María Cuevas-González, Michele Crosetto, and Oriol Monserrat. 2022. Classification of Ground Deformation Using Sentinel-1 Persistent Scatterer Interferometry Time Series. GIScience &

Remote Sensing 59 (1): 374–92. https://doi.org/10.1080/15481603.2022.2030535.

Montgomery, DR, K Sullivan, and HM Greenberg. 1998. Regional Test of a Model for Shallow Landsliding. Hydrol. Processes 12 (6): 943–55.

Oord, Aaron van den, Sander Dieleman, Heiga Zen, Karen Simonyan, Oriol Vinyals, Alex Graves, Nal Kalchbrenner, Andrew Senior, and Koray Kavukcuoglu. 2016. "WaveNet: A Generative Model for Raw Audio." arXiv. https://doi.org/10.48550/arXiv.1609.03499.

Savage, JC, JL Svarc, and WH Prescott. 2003. Near-Field Postseismic Deformation Associated with the 1992 Landers and 1999 Hector Mine, California, Earthquakes. Journal of Geophysical Research-Solid Earth 108 (B9). https://doi.org/10.1029/2002JB002330.
Schlögl, Matthias, Barbara Widhalm, and Michael Avian. 2021. Comprehensive Time-Series Analysis of Bridge Deformation Using Differential Satellite Radar Interferometry Based on Sentinel-1. ISPRS J. Photogramm. Remote Sens 172 (February): 132–46. https://doi.org/10.1016/j.isprsjprs.2020.12.001.

Schneider, Philipp J., and Uwe Soergel. 2021. Clustering Persistent Scatterer Points Based on a Hybrid Distance Metric. In Pattern Recognition, edited by Christian Bauckhage, Juergen Gall, and Alexander Schwing, 13024:621–32. Lect. Notes Comput. Sci.. Cham: Springer International Publishing. https://doi.org/10.1007/978-3-030-92659-5_40.

Tiwari, Ashutosh, and Manoochehr Shirzaei. 2024. A Novel Machine Learning and Deep Learning Semi-Supervised Approach for Automatic Detection of InSAR-Based Deformation Hotspots. International Journal of Applied Earth Observation and Geoinformation 126 (February): 103611. https://doi.org/10.1016/j.jag.2023.103611.

Wang, Liuyu, Kazhong Deng, and Meinan Zheng. 2020. Research on Ground Deformation Monitoring Method in Mining Areas Using the Probability Integral Model Fusion D-InSAR, Sub-Band InSAR and Offset-Tracking. International Journal of Applied Earth Observation and Geoinformation 85 (March): 101981. https://doi.org/10.1016/j.jag.2019.101981.

Li, Yingchen, and Ke Yinghai. 2015. Spatial-Temporal Heterogeneity of Land Subsidence Evolution in Beijing Based on InSAR and Cluster Analysis. In IET International Radar Conference 2015, 3 .-3 . Hangzhou, China: Institution of Engineering and Technology. https://doi.org/10.1049/cp.2015.1423.

Zhu, Wenxin, Fengming Hu, and Feng Xu. 2023. Post-Processing of InSAR Deformation Time Series Using Clustering-Based Pattern Identification. J. Beijing Inst. Technol. (Engl. Ed.) 32(6): 704–16. https://doi.org/10.15918/j.jbit1004-0579.2023.084.